

Mechanical properties of diamond lattice structures based on main parameters and strain rate

R. Miralbes^{a*}, N. Santamaria^a, D. Ranz^a and J.A. Garcia^a

^a *Department of Design and Manufacturing, University of Zaragoza, Zaragoza, Spain*

* miralbes@unizar.es. DIDYF-EINA. C/ Maria de Luna n. 4, 50018, Zaragoza (Spain).

Mechanical properties of diamond lattice structures based on main parameters and strain rate

The diamond triply periodic minimal surface structure has a high mechanical property–weight ratio. They can be modified by changing their internal parameters or the material. They are generated using the additive manufacturing (AM) that possibilities the use of various materials for generating zones with different mechanical properties or by modifying their internal parameters. However, the effects of internal parameters in the mechanical properties have not been defined in detail. Furthermore, the strain rate modifies these mechanical properties. In this study, the effects of the internal parameters and strain rate were evaluated and additionally, the failure mechanism of the structures.

Keywords: lattice; energy absorption; additive manufacturing; failure mechanism; compression; diamond.

Introduction

Traditionally, polymeric foams such as the expanded polystyrene (EPS) have been used to absorb energy in some applications, such as the automotive and packaging industries. An example is helmets that protect the brain from impact, as they have a significant ability to deform and absorb energy. Although these materials are petroleum based and have a non-renewable origin, they possess excellent properties: high energy absorption, low density, good economy, property modification during the manufacturing process, and the capability to form complex shapes. Thus, they are used in diverse applications, such as for producing seat cushions, bumper systems, and liners in helmets (for motorcyclists, field workers, and sportspeople) and side-impact protection systems.

Polymeric foams are manufactured during a foaming process in which foam expansion can be controlled to achieve the desired density. Studies [1, 2] have established a clear relationship between the density and the mechanical properties of different polymeric foams. Similarly, the foaming process generates closed cells inside

the material that traps the air; hence, the higher the density, the lower the trapped air and distance between the cell walls.

Other researchers [3] found that these materials exhibited a characteristic stress–strain relationship and developed a material behavior mode and also determined a material model called the Ashby–Gibson model to determine the main mechanical properties for main foams depending on the non-foamed original material and the relationship between the density of the foamed and of the solid material. The Ashby–Gibson observation divides the stress–strain curve into three well-defined parts: elastic, plateau, and densification zones. In the elastic zone, the material exhibits an elastic behavior and can recover its initial shape and size, and the stress–strain relationship is linear. The slope of this curve is the elastic Young’s modulus of the material. In this zone, the higher the density, the higher the elastic Young’s modulus because there is a large material volume. Subsequently, some internal cells of the structure start to collapse, and the plateau zone appears, which is defined by somewhat constant stress levels that typically increase slowly. This defines the plateau Young’s modulus. In the plateau zone, the higher density indicates a higher quantity of structural material, implying higher stress levels. The plateau zone optimally absorbs adequate energy without significantly increasing the stiffness.

Finally, the entire cells collapse, and no air remains trapped; thus, opposite cell walls contact. The stress increases sharply, and the mechanical properties are similar to those of the original nonfoamed material. This zone, called the densification zone, should be avoided in these applications because a high rigidity indicates high decelerations during an impact. In the case of a helmet, for instance, high decelerations

during an impact cause severe brain injuries [4]. This behavior mode and the relevant parameters are explained in detail in Section 2.3. A higher quantity of material and less air trapped inside suggest that opposite walls have contact with decreased material deformation.

Conversely, some parameters such as the geometry of the element must be considered when designing an effective energy absorber to protect and minimize the damage of different zones of the element. It is well known that for helmets [5], the stiffness of each part of the skull and the tolerance and functions controlled by each brain zone are different. Thus, the probability of impact on an area of the head during an accident varies [6]. Consequently, it is essential to adapt each zone of the energy absorber element to produce effective protective devices [7]. A study [8] investigated the effects of rotational decelerations and moments on brain damages caused by oblique impact and concluded that the low weight of the helmet is essential to reduce these moments. Although EPS has a low density, the manufacturing process limitations prevent its generation of one-part EPS energy-absorber elements, which can have different densities and mechanical properties. Therefore, it is necessary to search for alternative materials.

Some researchers have examined natural materials [9], such as cork and cork agglomerates [10], biocomposites [11], and mycelium basis materials [12]. Although these materials have renewable origin and could be easily recycled and/or decompose, they present the same limitation as the EPS: they cannot be tailored zone by zone to modify their mechanical properties.

Other researchers have investigated the additive manufacturing (AM) process [13]. This technique enables the application of different materials, such as renewable materials like acrylonitrile styrene acrylate (ASA), to produce multimaterial structures

[14]. It also possibilities the use different structures based on the zone with different mechanical properties and stiffness [15], modified thickness of the structure based on the zone [16], or the possibility to form gradient structures [17]. Consequently, different methods are used to generate zones with different mechanical properties tailored and optimized, for instance, in the case of helmets, to improve safety and reduce the weight

Different types of filling structures can be applied. Examples of such structures include the bioinspired [18], auxetic lattice [19], trust [20], prismatic tetrahedral [13], and triple periodic minimal surface (TPMS) structures. TPMS structures are widely known lattice structures and are invariant under a rank-3 tensor. They are intricate periodic scaffolds generated by repetitive basic cells defined using a mathematical function to generate thick surfaces for the final structure that could be named thickened triple periodic minimal surface (TTPMS). TTPMS structures have a relatively low density and a significant energy absorption capacity under compressive loads [21]. Thus, they are suitable substitutes for EPS because they could have similar mechanical properties per unit of weight or per unit of volume and similar behavior mode but allowing them to generate products different zones, each with different optimized stiffness that is impossible to generate with a foaming process. AM is suitable for modifying the mechanical properties of several materials, such as thermoplastics [22], stainless steel [23], titanium [24], and elastomers [25]. These structures exhibit similar behavior mode that the one described by the Ashby–Gibson observations [26].

Several TTPMS structures exist, but the most promising types in terms of low density and desirable mechanical properties are diamond, gyroid, Schwarz-P or primitive, Neovious, Lidinoid, and split-P [27–29]. These structures are controlled by two major parameters: basic cell length and wall thickness of the structures

Some researchers have compared different structures [30, 31]. A study [32] concluded that split-P, diamond, and Neovious have better mechanical properties and higher energy absorption per unit weight than other structures. Neovious structures have significantly higher stress levels in the plateau zone, but the densification zone appears with relatively low deformation [32]. For split-P and diamond structures, the stress levels are high and similar, but the split-P structure is more unstable than that of the diamond structure, and more oscillations appear on the stress–strain curve.

Additionally, the densification zone appears with a lower strain than in the case of the diamond. Hence, diamond structures are the most suitable for energy absorption applications. A study [33] on gyroid structures reveals that structures produced with ASA or ABS have similar properties with EPS structures.

The mechanical properties of any material, including TTPMS [34], vary depending on the velocity of the applied load. Hence, it is necessary to determine the load variation during impacts. For materials and structures consistent with the Ashby–Gibson observation, an increase in the strain rate, on the one hand, typically indicate increased stress levels in the plateau zone and an increase in Young’s modulus; on the other hand, the densification zone appears with a decreased strain [35].

In this study, the effects of the strain rate and internal parameters of ASA diamond structures on their mechanical properties and energy absorption capacity were investigated. This study gives a broad view of how these structures should be tailored to obtain desired mechanical properties in static and dynamic applications in substituting polymeric foams. In addition, diamond structures were compared with EPS foams used in helmets.

Materials and methods

Materials

ASA with the commercial name, Z-ASA Pro, manufactured by Zortrax, was used as the material in this study. It was used in a Zortrax M200 printer with a 0.4 mm nozzle to print all the specimens using the fused filament fabrication procedure, with a layer height of 0.19 mm.

The solid materials were subjected to compression according to the ASTM D1621 test method using three strain rates (0.0016 or quasistatic according to the standard, 0.0075, and 0.1 s⁻¹). The results, which were used for comparisons with the diamond structures, were processed to obtain the material curves and the main mechanical properties.

This study focused on a specific TTPMS structure, that is, the diamond, which has a significant energy absorption per unit mass [32]. This structure is consistent with the Ashby–Gibson observation [3]. N-Topology (version 3.21.2), a CAD and finite elements method software developed by the company with the same name, was used to generate the diamond structures, defined by Equation (1) [36]. N-Topology uses an approximation of this equation to generate TPMS surface.

$$F(x, y, z) = \sin\left(\frac{2\pi x}{a}\right) \sin\left(\frac{2\pi y}{a}\right) \sin\left(\frac{2\pi z}{a}\right) + \sin\left(\frac{2\pi x}{a}\right) \cos\left(\frac{2\pi y}{a}\right) \cos\left(\frac{2\pi z}{a}\right) + \cos\left(\frac{2\pi x}{a}\right) \sin\left(\frac{2\pi y}{a}\right) \cos\left(\frac{2\pi z}{a}\right) + \cos\left(\frac{2\pi x}{a}\right) \cos\left(\frac{2\pi y}{a}\right) \sin\left(\frac{2\pi z}{a}\right) - t \quad (1)$$

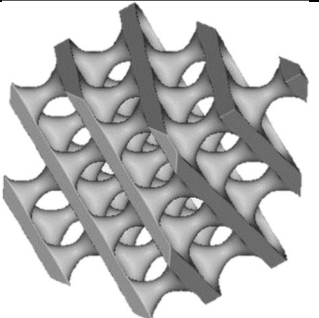
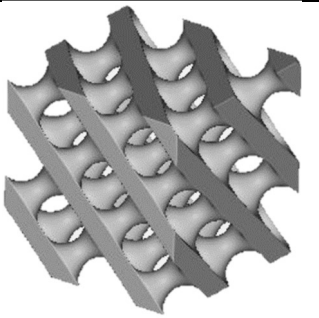
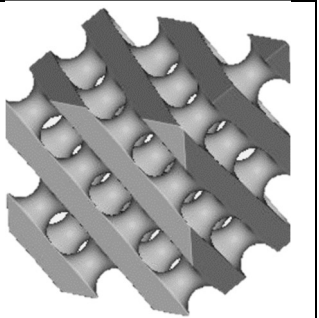
where x , y , and z are the coordinates, a is the cell size, and t is a constant adjusted for a desired wall thickness/volume fraction.

N-Topology and similar software generate TPMS-only surfaces initially without thickness, and the volume is subsequently generated using implicit functions to obtain a TTPMS. This implicit method is defined by the volume fraction (ρ^*) instead of the

thickness (t), the most common parameter for defining lattice structures. The volume fraction (ρ^*) is the percentage of solid material inside the structure. A close relationship exists between the parameter that defines the thickness, t , and the volume fraction [37]. Additionally, ρ^* is related to the measured densities of the structure (ρ_{struct}) and solid material (ρ_{solid}).

$$\rho^* = \left(\frac{Volume_{struct}}{Volume_{solid}} \right) = \left(1 - \frac{\rho_{struct}}{\rho_{solid}} \right) \quad (2)$$

The aim of this study is to analyze the effects of the strain rate and main internal parameters on the mechanical properties of the diamond structure. Thus, the influence of the volume fraction and cell size was investigated, varying the cell size (6.6, 10, and 20 mm) and volume fraction (20%, 30%, and 40%; Figure 1); this variation was made adjusting t and analyzing the volume of the specimen until the desired final volume fraction is obtained; whilst it could be generated a model that related directly t and the volume fraction, in this case the used method was more cost-effectively. The cell sizes and volume fractions were selected based on the manufacturing limitations and three-dimensional printer resolution, with six, four, and two cells inside the specimen. Finally, 40 mm × 40 mm × 40 mm cubic specimens where used; next section explains the reasons to use these dimensions. Although the specimen with two cells underwent relative distortion because of the low number of cells and the boundary effects[38], it was selected because of the limitations of the printing process and test machine and to obtain more graphical points.

ρ^* vs. t	20%	30%	40%
20 mm			

10 mm			
6.6 mm			
Density (kg/m ³)	210	315	420

Figure 1. CAD model of the different diamond specimens in function of the volume fraction and the period

The nomenclature used for each diamond specimen was “X_YY,” where X is the number of cells, and YY is the volume fraction. For the EPS, the density was 120 kg/m³, and it was named “EPS.” For the solid ASA material, the name was “Solid.”

Methods

The materials were subjected to dynamic and quasistatic compressive loads using an 8032 Instron universal testing machine. Although a specific standard for testing such TTPMS structures has not been developed, the standard for cellular foams was adopted [33] because of the similarity in the mechanical behaviors of TTPMS structures and cellular foams, such as polyurethane (PUR) and EPS. Consequently, ISO 844 – “Rigid Cellular Plastics Compression Properties,” ASTM 3574 – “Standard Test Methods for Flexible Cellular Materials: Slab, Bonded, and Molded Urethane Foams,” and ASTM D1621 – “Standard Test Method for Compressive Properties of Rigid Cellular Plastics,”

can be used for quasistatic tests. The main difference between these standards is the dimension of the specimen. The specimen recommended by ISO 844 is a 50 mm × 100 mm × 100 mm prism, and its minimum thickness is 50 mm. For the ASTM 3574 specimen, no minimum thickness is specified, and the size is 50 mm × 50 mm × 25 mm. The minimum size of the ASTM D1621 specimen is 25.4 mm × 25.4 mm × 25.4 mm. Because of the Instron maximum load capacity (100 kN), a 40 mm × 40 mm × 40 mm prism specimen was used, and ASTM D1621 was adopted. Additionally, a solid 25.4 mm × 25.4 mm × 25.4 mm prism specimen was evaluated to characterize the original material.

These codes specify the same movement condition for the strain rate: the crosshead displacement rate must equal 10% of the sample thickness per minute. Thus, the velocities for the TTPMS and solid prisms were 4 and 2.54 mm/min, respectively, indicating a strain rate of 0.0016 s^{-1} in both cases.

No universal code for the dynamic testing of this or other similar materials has been developed. Therefore, ASTM D1621 was adopted, but with different velocities; the maximum velocity was determined based on the maximum velocity of the Instron machine (4 mm/s) applied to the TTPMS specimen, implying a strain rate of 0.1 s^{-1} . An intermediate strain rate of 0.0075 s^{-1} (a test velocity of 0.3 mm/s) was applied. Therefore, 2.54 and 0.1905 mm/s test velocities were applied to obtain the same strain rate for the solid materials.

The uniaxial testing machine recorded the forces and displacements during the tests. The values were used to plot the stress (σ)–strain (ε) curves based on the dimensions of the specimen. The absorbed energy per unit volume (W)–strain curve was plotted using Equation (3), and based on the density, the specific stress (σ_s)–strain and absorbed energy per unit volume (W_s)–strain curves were plotted.

$$W = \int_0^{\varepsilon} \sigma(\varepsilon) d\varepsilon \quad (3)$$

$$W_s = \frac{W}{\rho_{struct}} \quad (4)$$

$$\sigma_s = \frac{\sigma}{\rho_{struct}} \quad (5)$$

The absorbed energy can be divided into two energies: the absorbed elastic energy that can be recovered (Equation (6)) and the plateau energy that cannot be recovered (Equation (7)).

$$W_e = \int_0^{\varepsilon_{c,d}} \sigma(\varepsilon) d\varepsilon \quad (6)$$

$$W_p = \int_{\varepsilon_{c,d}}^{\varepsilon_{c,p}} \sigma(\varepsilon) d\varepsilon \quad (7)$$

Ashby-Gibson observation and its parameters

Ashby and Gibson [3] investigated the mechanical properties of polymeric foams under compression. They observed that these materials exhibited a characteristic stress–strain behavior, and a relationship existed between the density and the values of this curve. Thus, they established a material behavior mode for these types of structures. These mechanical properties can be modified by controlling the density during the foaming process [1, 2]. Some researchers concluded that this behavior mode applies to corks and cork products [10] and lattice structures [17].

The Ashby–Gibson observation defines three well-defined zones in the stress–strain curve. In the first zone, called the linear zone, the material exhibits a linearly elastic behavior, and the slope of the curve defines Young’s modulus of the material. In the linear zone, the material or structure can recover its initial shape. After a certain point, the cells start to collapse, and a deviation of the actual curve larger than 0.2% of the elastic curve is observed; at this point, the plateau zone appears, and the material or structure cannot recover its initial shape. In the plateau zone, different types of the

collapse of the structure and cell may occur, depending on several factors (such as the material, type of TTPMS structure, and parameters of the structure) [32]. The structures and cells collapse progressively; hence, this zone has somewhat constant or increasingly mild stress levels. The average stress value in this zone defines the plateau modulus.

Subsequently, the opposite cell walls contact, and the densification zone appears. The stress increases steeply, and for a TTPMS structure, it behaves like a solid material (Figure 2).

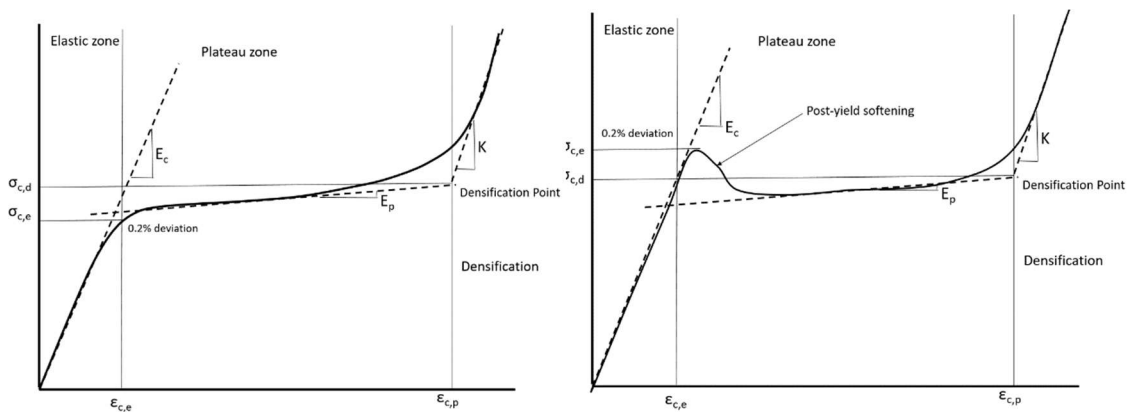


Figure 2. Ashby-Gibson behavior modes for bending (left) and for stretching-dominated structures (right)

The Gibson–Ashby observations establish that foams exhibit either of two behaviors after plasticity commences, depending on whether the cell collapse is dominated by bending or stretching. Therefore, the deformation mechanisms are different. In stretch-dominated structures, the initial collapse strength and elastic modulus are high but decrease in the plateau zone because post yield softening occurs; thus, this case is ideal for lightweight structures in the elastic zone. In bending-dominated structures, there is no local peak when plasticity starts, and the stress in the plateau zone is almost equal to the initial collapse strength. Hence, these structures are suitable for applications that require the plateau zone to absorb energy. Alomar and Concli [39] concluded that TTPMS structures exhibit similar behavior.

The main parameters determined from these curves are as follows: the maximum tensile strength in the elastic zone ($\sigma_{c,e}$), maximum tensile strength in the densification point ($\sigma_{c,d}$), maximum elastic elongation ($\varepsilon_{c,p}$), elongation in the densification point ($\varepsilon_{c,d}$), elastic Young's modulus (E_c), plateau Young's modulus (E_p), densification Young's modulus (E_d). E_c can be used to determine the maximum elastic elongation ($\varepsilon_{c,p}$) when a deviation higher than 0.2% of the elastic curve appears. This point defines $\varepsilon_{c,p}$ and $\sigma_{c,e}$.

For $\varepsilon_{c,d}$ and $\sigma_{c,d}$, this point is determined from the intersection between the line defined by the slope of the plateau zone (E_p) and a tangent curve in the densification zone. The tangent curve in the densification zone is plotted using the bulk modulus of the solid material (K) for the TTPMS structure and, in the case of foams, the bulk modulus of the nonfoaming material.

The density (ρ) can be used to determine specific properties; these properties are the ratios of the previous parameters to the density. Nonspecific parameters are used to compare different structures and/or structures with the same volume, whereas specific parameters are used to compare structures and/or materials with the same weight. Thus, the following parameters are determined: the maximum specific tensile strength in the elastic zone ($\sigma_{cs,e}$), maximum specific tensile strength in the densification point ($\sigma_{cs,d}$), specific elastic Young's modulus (E_{cs}), specific plateau Young's modulus (E_{ps}), specific elastic absorbed energy (W_{es}), and specific energy absorbed in the plateau zone (W_{ps}).

The primary use of TTPMS structures is the kinetic energy dissipation of a shock through energy absorption. Nevertheless, it is essential to maintain the maximum force, deceleration, or both below a limit, depending on the application. Thus, these materials should be modified to achieve an optimal behavior. For foams [40], the

control of the density during foaming influences the mechanical properties; in the case of TTPMS structures, volume fraction control is critical.

At this point, it is essential to explain the influence of the stress–strain curve on the deceleration process and maximum force. If the structure is insufficiently stiff across the curve, particularly in the plateau zone (low W_p and low $\sigma_{c,e}$), the densification point, $\epsilon_{c,d}$, is exceeded on impact, and the densification zone appears. Consequently, the stiffness increases sharply, implying high decelerations and forces. Therefore, severe brain injuries (in the case of helmets) and breakage of packaged goods may occur. However, excessively stiff (high $\sigma_{c,e}$) structures may generate high decelerations and forces initially with the same final results but with a lower final strain, indicating that the material is only partially crushed. For the optimal use of the structure, the objective is to utilize the entire plateau zone without reaching the densification point.

Mechanical tests were repeated 3 times for all volume fractions cell sizes and strain rates. Only small deviation of the results were observed in the stress strain curves as confirmed by the groups previous studies [10, 17, 32, 33] (a selection of some of the results of the study of the variability are shown in Table 1). The low deviation could be due to aspects such as the control of the temperature of the room and of the printing space, the use of the same roll of material for the identical specimens, the use of the same printing machine and that the specimens have been printed and tested consecutively. Furthermore, the same printing parameters, nozzle, etc. were used that probably reduces the influence of the manufacturing process and of the environment in the variability of the results. Finally, due to the low observed deviation, it has been used in this work the first specimen tested.

Table 1. Analysis of the deviation of the results for some specimens

Cells	ρ^* (%)	Strain rate (s^{-1})	Specimen	E_c	$\sigma_{c,e}$	$\sigma_{c,p}$	$\sigma_{c,d}$	$\epsilon_{c,e}$	$\epsilon_{c,p}$
				MPa				%	

2	20	0.0016	1	26.8	1.4	1.1	0.9	5.2	63.4
			2	28.1	1.5	1.2	0.9	5.1	64.5
			3	26.4	1.3	1.1	1.0	5.4	66.5
Deviation (%)				6.0	13.3	8.3	10.0	5.6	4.7
4	30	0.075	1	72.0	4.1	3.8	5.2	5.7	51.2
			2	69.0	4.2	3.9	5.5	5.8	50.6
			3	73.3	4.0	3.8	5.3	5.7	52.7
Deviation (%)				5.9	4.8	2.6	5.5	1.8	4.0
6	40	0.1	1	122.0	7.8	7.0	10.0	6.4	56.0
			2	131.0	8.3	7.3	9.3	6.7	56.5
			3	119.0	7.6	6.9	9.6	6.3	53.2
Deviation (%)				9.2	8.4	5.5	7.0	6.0	5.8

Other variables of interest

Miltz [41] proposed another method for obtaining results using the efficiency parameter (W). This additional indicator, typically plotted against the strain, is defined as the ratio of the absorbed energy to the stress.

$$W = \frac{\int_0^{\varepsilon} \sigma(\varepsilon) d\varepsilon}{\sigma} \quad (8)$$

Some previous studies on foams [42] and cork products [10] have revealed that a typical efficiency–stress diagram always has a maximum because, after a certain point, the rate of increase in the absorbed energy is lower than the rate of increase in the stress.

Although efficiency is a valuable parameter for materials characterized by a monotonically increasing stress–strain curve, some researchers [43, 44] have revealed that its need in other cases is questionable. In these cases, if a sufficiently high maximum stress peak is attained in the early stage, the material reaches a stress level that must be considered instead of the stress for each strain. Here, the total efficiency (W_t) is a more appropriate indicator, and it is the ratio of the energy to the maximum stress. For monotonically increasing materials, the efficiency and total efficiency are identical.

$$W_t = \frac{\int_0^\varepsilon \sigma(\varepsilon) d\varepsilon}{\max_{0 \leq x \leq \varepsilon} \sigma} \quad (9)$$

The ideality (I) is another indicator defined by Miltz [41].

$$I = \frac{\int_0^\varepsilon \sigma(\varepsilon) d\varepsilon}{\sigma \varepsilon} \quad (10)$$

Ideality reflects the stress and strain at each point in analyzing how close a structure is to an ideal absorber (an absorber with constant stress along with the strain). However, Miltz [41] observed that in most cases, ideality yields a nonoptimal solution, owing to the typical shapes of stress–strain curves. Hence, the maximum ideality typically appears at the end of the elastic zone. The material exhibits small deformation, indicating that the energy-absorbing ability of the plateau zone is unused. Hence, this indicator was discarded.

Another approach for analyzing the TTPMS of different materials is the normalized form [30, 45]. Here, a double-logarithmic diagram is plotted to present the absorbed energy divided by the elastic modulus of the original solid under elastic compression vs the stress divided by the elastic modulus of the solid material. In this case, only a solid material with the same elastic modulus is used. Thus, the shape of the plotted diagram would be identical to the absorbed energy vs stress diagram.

Rush [46] established a material model different from the Gibson–Ashby model for foams and similar materials that use other indicators, such as the cushion and Jansen factors. However, the complexities involved in the mechanical characterization of the Rush model limits its application.

Results and discussion

Analysis of effect of volume fraction

Figure 3 shows the stress–strain curves of all the specimens, and Table 2 lists the main mechanical properties. An increase in the volume fraction increased the stress level in the plateau zone, maximum stress in the elastic zone, and maximum specific tensile strength at the densification point. However, the densification zone appeared earlier with a decrease in strain. This behavior was observed for all the evaluated strain rates.

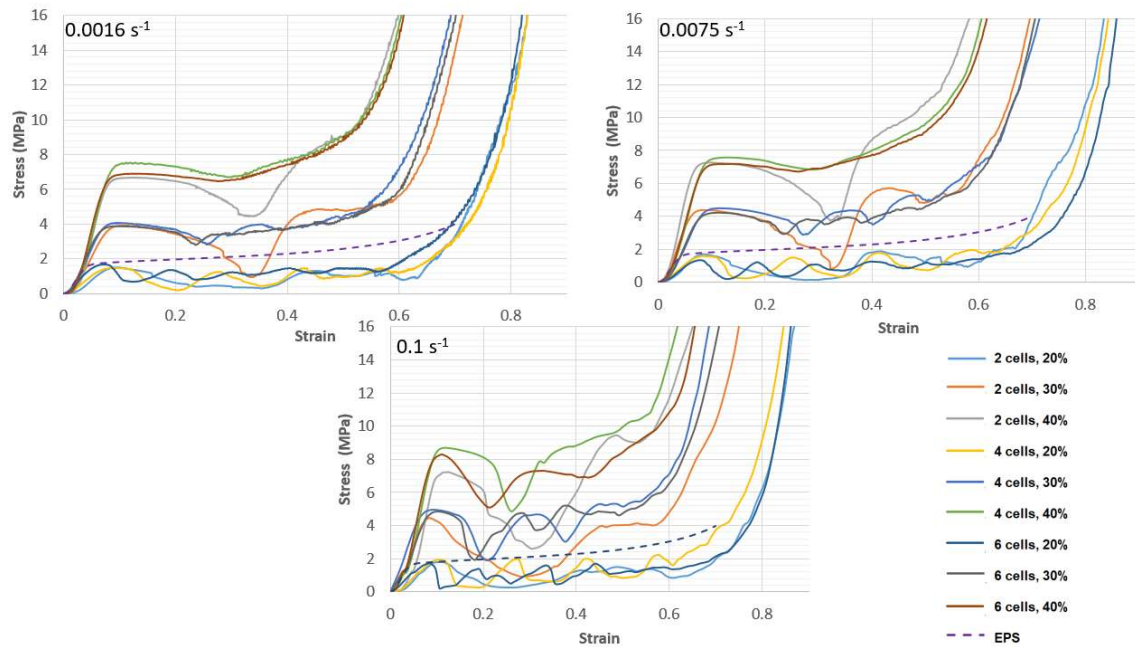


Figure 3. Stress-strain curve for the different specimens and strain rates

Table 2. Main mechanical properties of the studied specimens under different strain rates.

0.0016 s ⁻¹										
Cells	ρ^*	E_c	$\sigma_{c,e}$	$\sigma_{c,p}$	$\sigma_{c,d}$	$\epsilon_{c,e}$	$\epsilon_{c,p}$	W_e	W_p	$W_{t,max}$
		MPa			%		J/mm ³		%	
2	20%	26.8	1.4	1.1	0.9	5.2	63.4	3.7E-06	6.7E-04	35.9
	30%	59.4	3.7	2.6	5.1	6.2	59.3	1.2E-05	2.2E-03	37.1
	40%	126.8	6.2	5.6	9.0	4.9	51.1	1.5E-05	3.2E-03	32.6
4	20%	25.1	1.4	1.1	1.4	5.6	61.7	3.9E-06	7.2E-04	39.8
	30%	72.8	3.8	3.3	4.8	5.2	53.2	9.9E-06	1.8E-03	39.5
	40%	132.0	6.5	7.0	9.0	4.9	51.3	1.6E-05	3.6E-03	37.0
6	20%	36.8	1.6	1.2	1.5	4.3	58.4	3.1E-06	6.7E-03	41.2
	30%	72.2	3.8	3.4	5.0	5.3	57.8	1.0E-05	2.0E-03	39.9
	40%	134.2	7.2	6.6	9.0	5.4	52.2	1.9E-05	3.6E-03	36.2
0.0075 s ⁻¹										

Cells	ρ^*	E_c	$\sigma_{c,e}$	$\sigma_{c,p}$	$\sigma_{c,d}$	$\epsilon_{c,e}$	$\epsilon_{c,p}$	W_e	W_p	$W_{t,max}$
		MPa				%		J/mm ³		%
2	20%	34.5	1.6	1.0	2.0	4.6	67.3	3.7E-06	6.5E-04	33.3
	30%	91.0	4.0	3.0	5.2	4.4	58.4	8.8E-06	2.2E-03	37.1
	40%	141.0	6.8	6.0	11.0	4.8	47.2	1.6E-05	3.5E-03	30.8
4	20%	27.6	1.5	1.0	1.8	5.4	63.4	4.1E-06	4.7E-04	34.6
	30%	72.0	4.1	3.8	5.2	5.7	51.2	1.2E-05	1.8E-03	38.4
	40%	121.0	6.8	7.2	10.0	5.6	49.9	1.9E-05	3.3E-03	35.7
6	20%	24.6	1.2	0.9	1.8	4.9	66.7	2.9E-06	6.7E-04	37.4
	30%	70.5	4.2	3.6	4.8	6.0	55.3	1.3E-05	2.0E-03	39.0
	40%	119.0	6.8	7.0	10.0	5.7	52.3	1.9E-05	3.4E-03	36.5
0.1 s⁻¹										
Cells	ρ^*	E_c	$\sigma_{c,e}$	$\sigma_{c,p}$	$\sigma_{c,d}$	$\epsilon_{c,e}$	$\epsilon_{c,p}$	W_e	W_p	$W_{t,max}$
		MPa				%		J/mm ³		%
2	20%	23.5	1.7	1.0	1.7	7.2	62.6	6.1E-06	6.9E-04	36.9
	30%	69.0	4.2	3.0	4.0	6.1	60.2	1.3E-05	1.5E-03	35.5
	40%	140.0	6.9	6.0	9.0	4.9	53.3	1.7E-05	2.0E-03	32.2
4	20%	23.3	1.9	1.1	1.5	8.2	61.3	7.7E-06	5.3E-04	31.9
	30%	66.1	4.6	3.6	5.4	7.0	50.2	1.6E-05	1.9E-03	39.6
	40%	112.0	8.0	7.2	10.2	7.1	57.8	2.9E-05	3.9E-03	38.7
6	20%	22.7	1.8	1.0	1.9	7.9	63.3	7.1E-06	8.5E-04	42.5
	30%	63.3	4.6	3.6	5.0	7.3	57.2	1.7E-05	2.3E-03	40.9
	40%	122.0	7.8	7.0	10.0	6.4	56.0	2.5E-05	3.9E-03	38.8

Similarly, an increase in the volume fraction indicated an increased elastic Young's modulus. The absorbed energy analysis (Figure 4) revealed that the higher the volume fractions, the higher the energy absorption capacity at the same strain. This trend was observed for the elastic absorbed energy and the energy absorbed before densification.

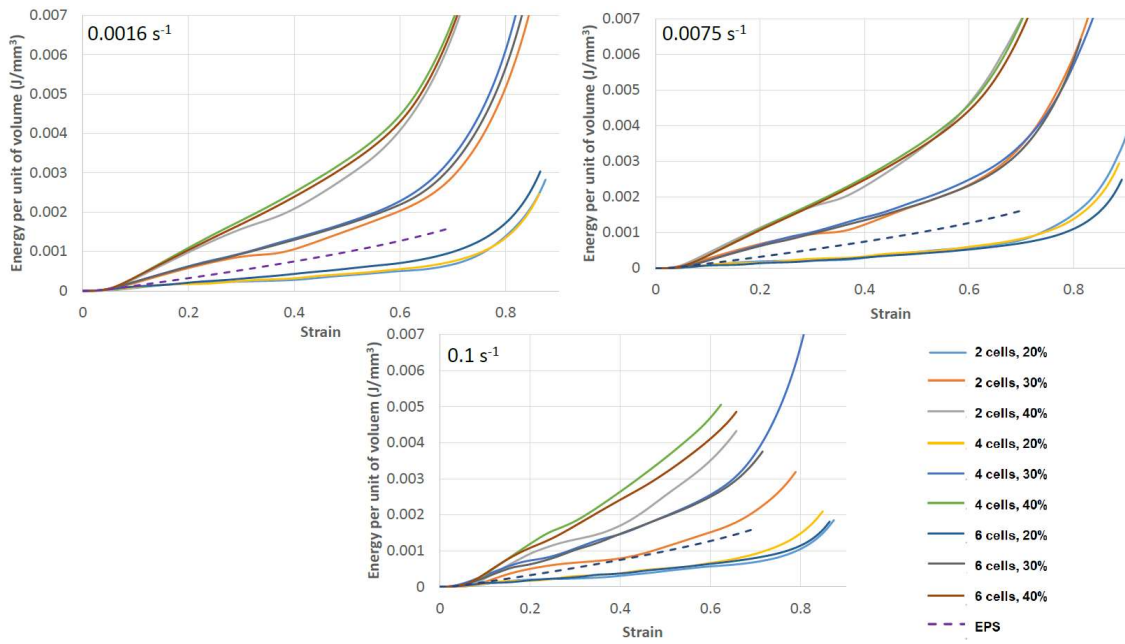


Figure 4. Energy absorption per unit of volume diagrams for the different specimens and strain rates

The lower volume fraction could, in some cases, imply a higher compression of the material. In the case of a helmet, this causes lower decelerations on the head, minimizing brain damage.

The analysis of properties per unit weight instead of per unit volume (Figures 5 and 6; Table 2) showed similar behavior. Although the difference in the stress magnitude decreased, an increase in the volume fraction resulted in increased specific elastic modulus and specific stress level.

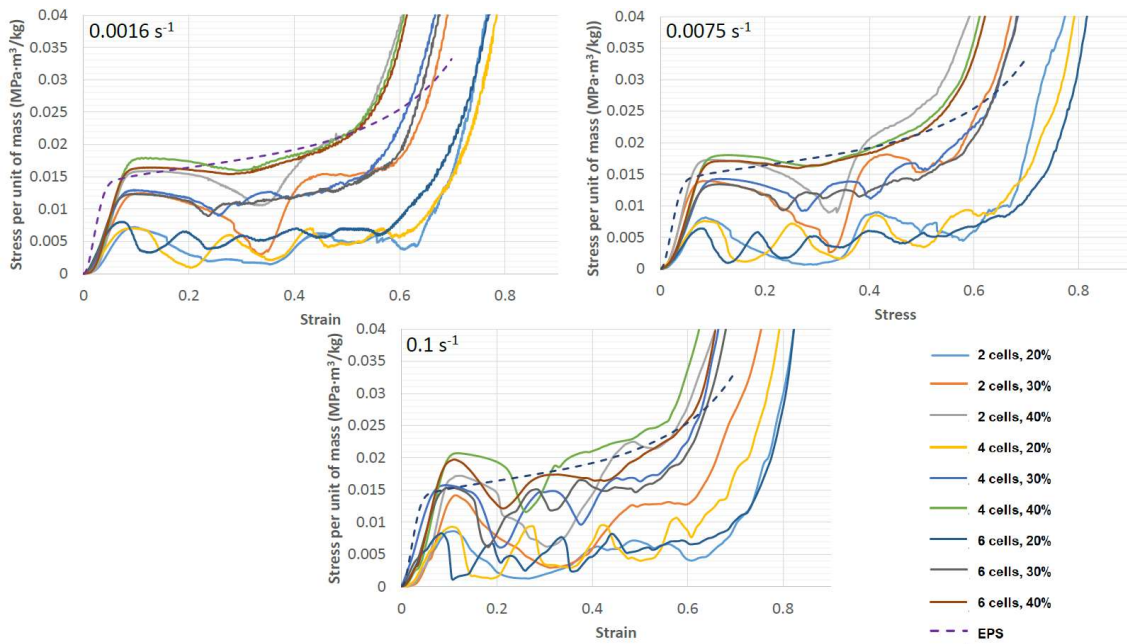


Figure 5. Specific stress-strain curve for the different specimens and strain rates

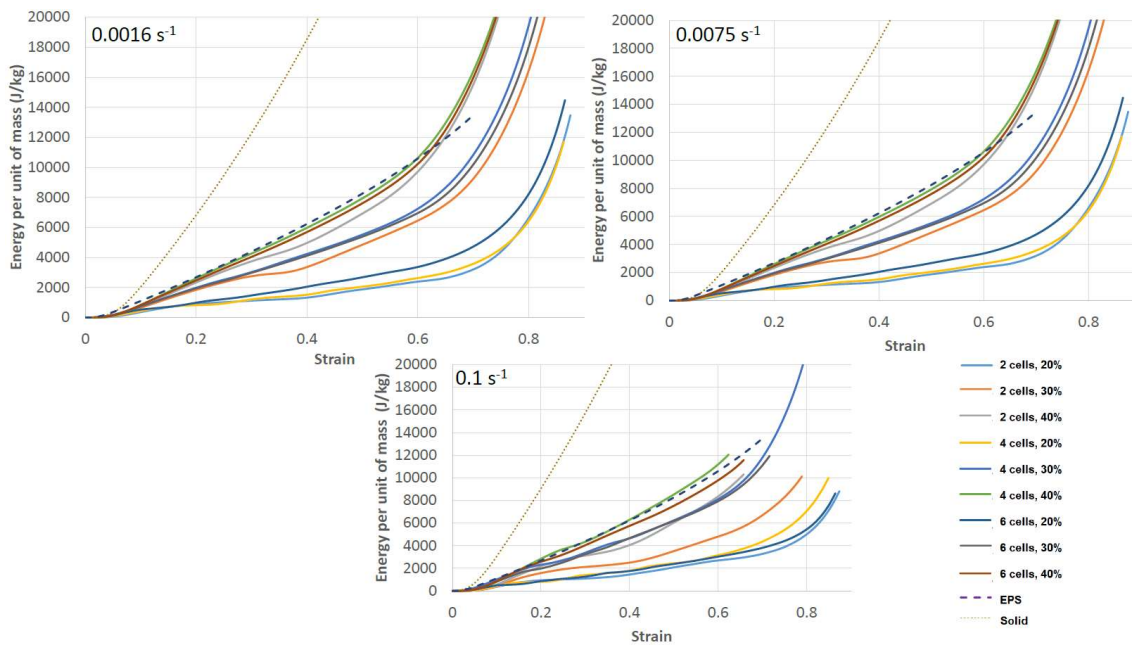


Figure 6. Energy absorption per unit of mass diagrams for the different specimens and strain rates

In terms of total effectivity (Figure 7), an increased volume fraction indicated increased stress at the maximum effectivity point. However, the relationship between the volume fraction and maximum total effectivity is unclear.

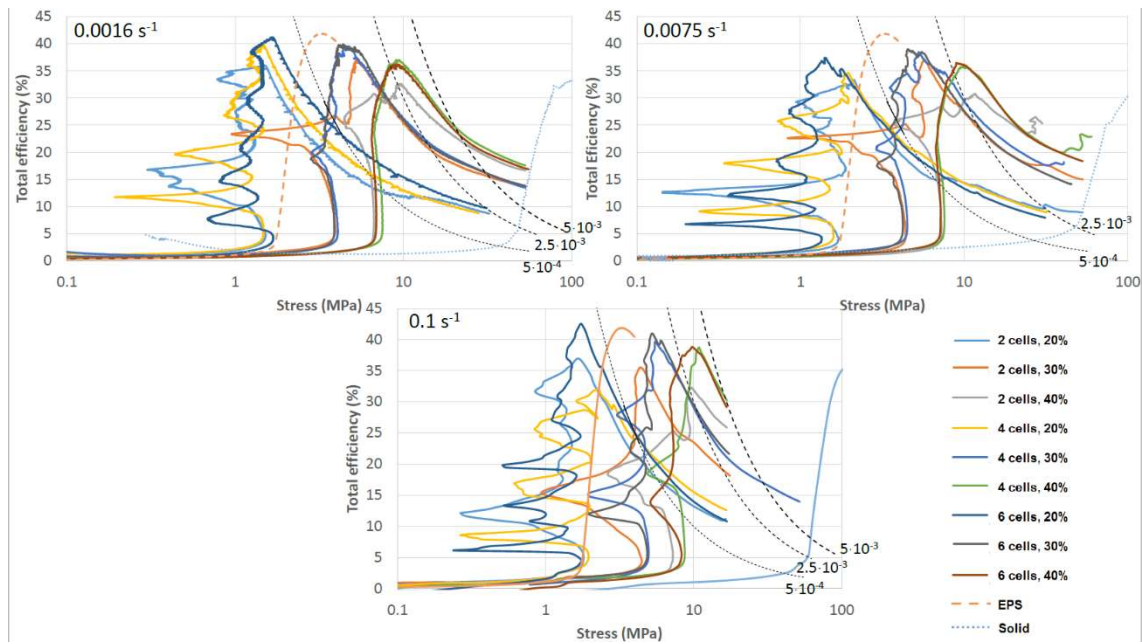


Figure 7. Total efficiency vs stress diagrams for the different specimens and strain rates with different iso-energy curves (dashed lines).

Analysis of effect of period

The analysis of the variable period (Figure 3 and Table 2) revealed a slight influence of this variable on mechanical behavior. The stress levels ($\sigma_{c,e}$, $\sigma_{c,p}$, $\sigma_{c,d}$) and densification point were similar for all specimens, but the trend is unclear. The number of cells somewhat influenced the shape of the stress–strain curve but there is not a direct relationship between the length of the unit cell and the mechanical properties. For the specimen with two cells, a decrease in values was observed for all cases corresponding to the cell collapse but this could be due to the boundary effects because two cell specimen is especially sensible to this aspect. In the case of four cells with a relative density of 20%, four waves in the curve matched with the number of cells; a similar observation was made for the specimen with six cells. This behavior occurred because the structure failed layer-by-layer diagonally. For the high relative densities (30% and 40%), these waves were not significant and disappeared because of the more abrupt

collapse in the lowest relative density specimen (attributed to the increased quantity of air inside).

The energy absorption analysis (Figure 4) reveals a similar energy absorption capacity. However, in the four-cell specimens, the densification appeared at lower strains, inducing earlier energy absorption.

For high strain rates, significant differences in the stress levels ($\sigma_{c,e}$, $\sigma_{c,p}$, $\sigma_{c,d}$) and energy absorption capacity were observed in function of the length of the cell size, particularly for the two-cell specimens but this could be due to the boundary effect. However, it has been observed that the lower the cell size, the higher the stress levels. It has been observed also that in some cases, for this strain ratio, specimens with lower volume fraction have the same capability to absorb energy than others with higher so, for high strain rates both parameters, cell size and volume fraction have influence in the capability to absorb energy. The analysis of the effectivity (Figure 7) indicated that a higher number of cells increased the total efficiency for all the strain rates.

Analysis of effect of strain rate

The analysis of the strain rate effect (Fig. 8) shows that an increase in the strain rate worsens the unstable behavior of the material, particularly at a 30% and 40% volume fraction reflected in more peaks and valleys in the curve. For 20% volume fraction at all strain rates, the number of peaks is independent of the strain rate; however, the 0.1 s^{-1} strain rate yielded slightly higher peaks and amplitudes of the curve oscillation associated with the collapse of each layer.

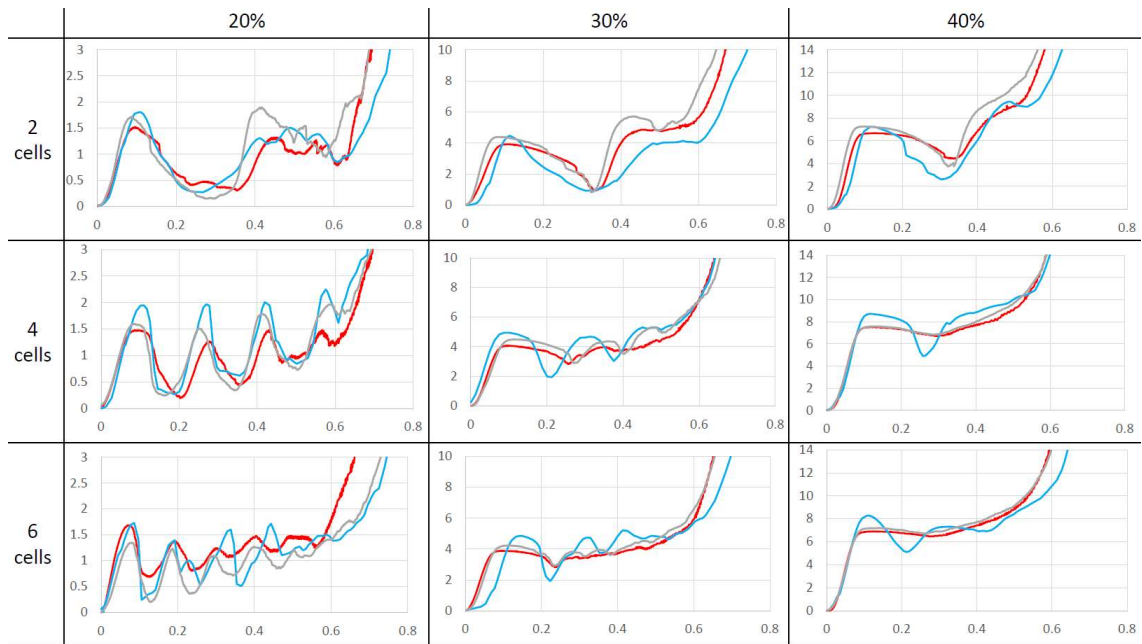


Figure 8. Stress-strain curves for different specimens [Stress (MPa) vs. strain]. Red: 0.0016 s^{-1} ; Grey: 0.0075 s^{-1} ; blue: 0.1 s^{-1}

In most cases, the higher the strain rate, the higher the maximum peaks and the oscillation amplitude. However, for the highest volume fraction and specimens with four or six cells, the behavior for the quasistatic condition and 0.0075 s^{-1} strain rate test were hardly equal. In the other cases, the 0.0075 s^{-1} strain rate showed slightly higher maximum values and amplitude ranges than the other strain rates. For the maximum strain rate, significant differences with the other strain rates were observed; however, the higher the volume fraction, the more similar the curves were with the other strain rates.

The analysis of the different parameters (Table 2) indicates an unclear relationship between the strain rate and the analyzed parameters. For the analysis of the energy absorption capacity before densification (Figure 9 and Table 2), the strain rate did not influence the higher volume fractions (30% and 40%) and the high number of cells (four and six). In the other case, although a medium strain rate (0.0075 s^{-1}) indicated a low number of cells and the highest capability to absorb energy, the highest

strain rate (0.1 s^{-1}) indicated the lowest. In the case of the lowest volume fraction, is the trend is unclear.

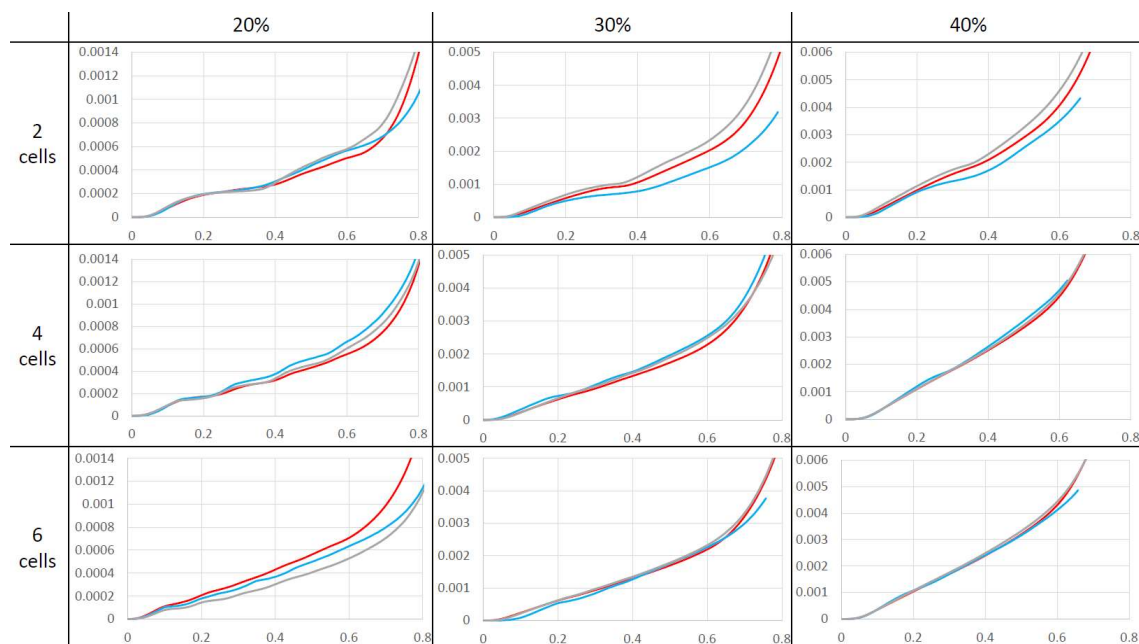


Figure 9. Energy absorption diagrams for different specimens [Energy (MJ/mm^3 vs. strain)]. Red: 0.0016 s^{-1} ; Grey: 0.075 s^{-1} ; blue: 0.1 s^{-1}

Analysis of effect of failure mode

A digital camera with an intervalometer was used to capture photographs at every 3% strain during the quasistatic test. A video camera was used in the dynamic load case to analyze the failure modes and their relationships with the stress–strain curve.

Cracks appeared in the cells at the center of the specimen and in the zone with less material (Figures 10 and 11). Subsequently, cracks appeared and propagated diagonally (red lines in Figure 12). Finally, the structure collapsed in this diagonal direction. This collapse slightly decreased the stress level with a decreased or increased strain, depending on the number of cells: the higher the number of cells, the lower the strain.

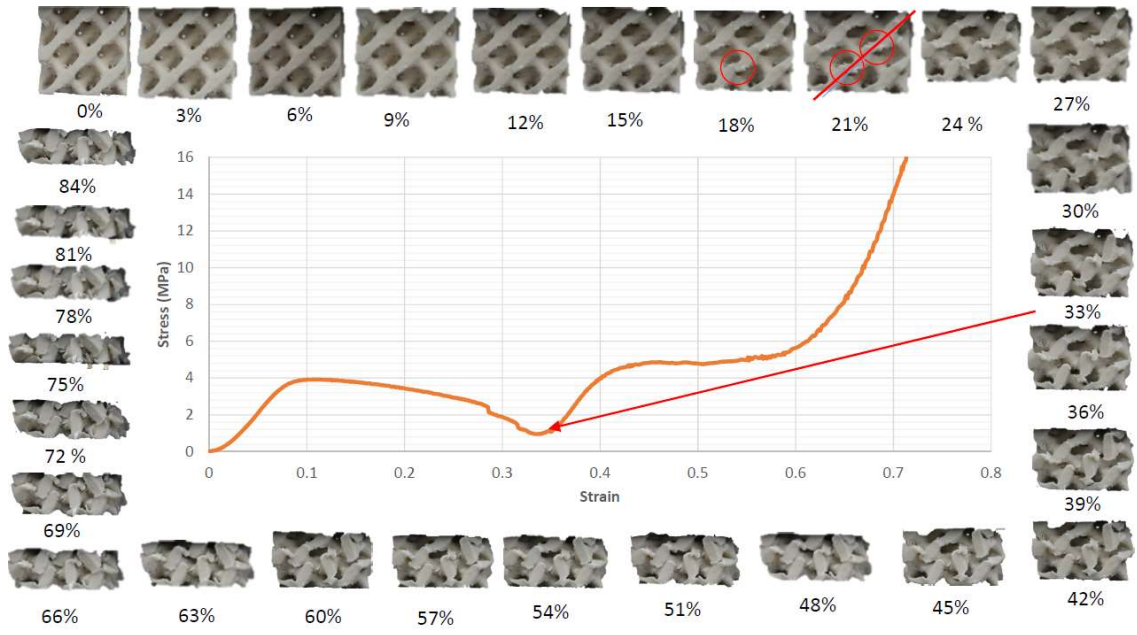


Figure 10. Stress-strain curves a 30% volume fraction and 2 cells specimen under quasi-static test.

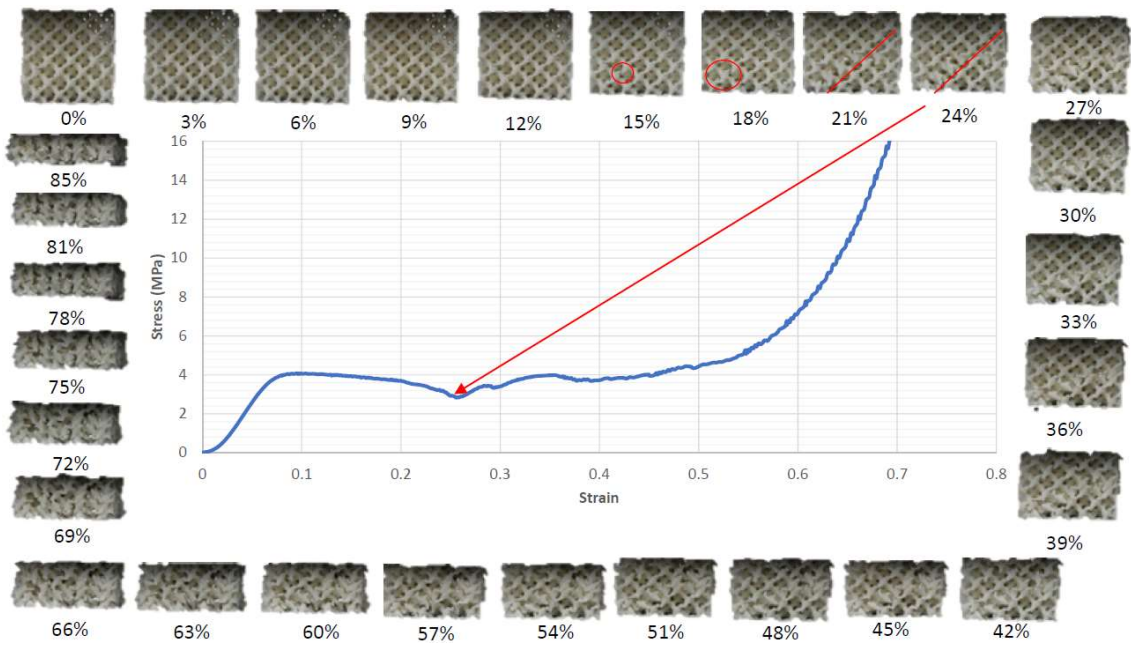


Figure 11. Stress-strain curves a 20% volume fraction and 4 cells specimen under quasi-static test.

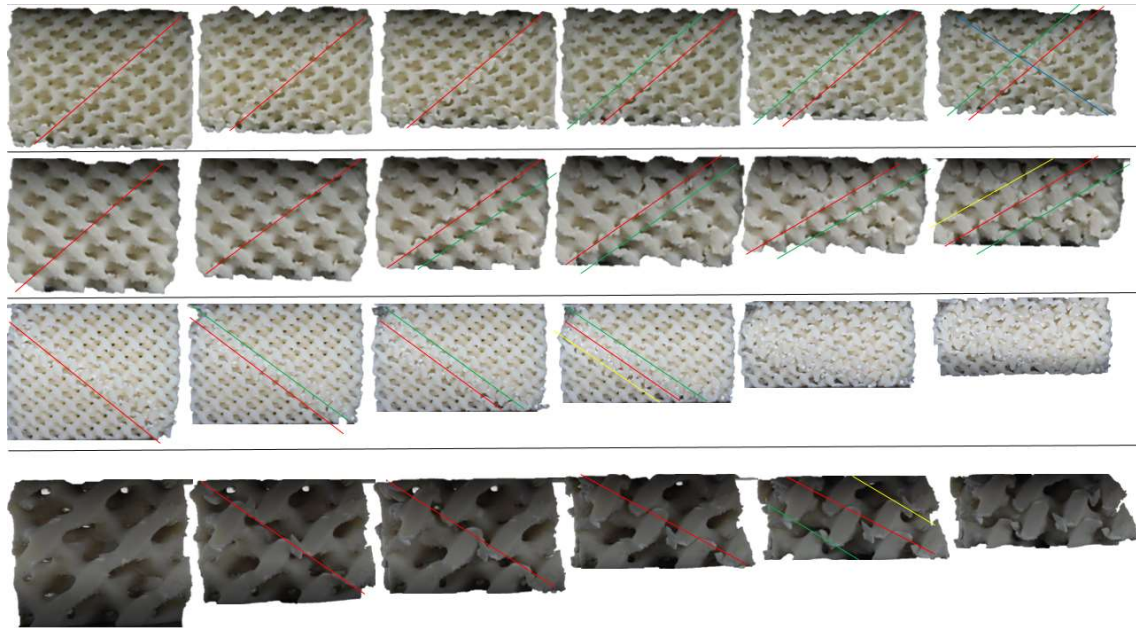


Figure 12. Different specimen's failure modes.

Next, the stress level recovered and increased progressively, and diagonal collapse occurred in the other cells outside. In some cases, this induced a new collapse in other diagonal directions but parallel to the initial collapsed cells (green and yellow lines in Figure 12). A collapse also occurred in the other diagonal (blue lines in Figure 12), called failure in "X." Finally, a material collapse occurred through a combination of layer-by-layer horizontally, layer-by-layer diagonally, and X-collapse.

Conclusions

This paper is a valuable reference for diamond TTPMS structures. The effects of the strain rate and internal parameters on the mechanical behavior and energy absorption capacity were investigated.

The results show that the volume fraction significantly influences both properties per unit weight and per unit volume. However, an increased volume fraction decreases the air quantity inside the structure, crushing the different cell walls together

earlier, and hence, the densification zone appears earlier. These findings are consistent with those reported by other authors [33, 47].

No clear relationship exists between effectivity and maximum effectivity. However, a decrease in the volume fraction decreases the stress levels, and the maximum effectivity appears at a decreased stress because the maximum total effectivity point typically appears near the densification point, consistent with a study [41].

The number of cells or the period did not significantly influence the properties. However, an increase in the period was caused by a decrease in the number of cells, indicating a significant decrease in the stress level for failure inside the cells. Additionally, these reductions increased with increasing strain because some cells collapsed earlier with an increasing number of cells.

The strain rate modifies the mechanical properties but does not modify the energy absorption capacity in most cases. The highest strain rates indicate high peaks and drops in the curve; consequently, the energy absorption trend is similar. Nevertheless, high strain rates indicate unstable stress–strain curves with significant oscillations, such as in gyroid structures [48].

The analysis results of the failure mechanism showed that in all cases, initial failure occurred in one of the main diagonals of the structure, consistent with [49]; after this diagonal collapses, the adjacent diagonals usually collapse. The collapse of the first diagonal is typically reflected in the stress–strain curve with a decrease in the stress level. However, the collapse of subsequent diagonals was not reflected in the curve. Finally, different failure mechanisms were observed, such as the X- and layer-by-layer failures, depending on the structure.

The properties of diamond structures can be modified based on the volume fraction. A sufficiently high number of cells in the structure is desirable to minimize the fluctuating stress levels. However, this is impossible in some cases because of the AM process resolution. Although the strain rate does not influence the energy absorption capacity, a high strain rate indicates high peak stress levels. Significant undulations of the stress–strain curve indicate high decelerations. In the case of a helmet, for instance, significant head damages may occur, but this should be investigated via tests on full-model helmets.

Finally, it must also be highlighted that this study has been made with loads applied in the printing direction. However, due to the influence of this parameter and the influence of the crystallographic orientation of the final structures, results could vary in function of this aspect that should be also studied in the future.

Acknowledgements

The authors would like to thank nTopology company that provided the software that was essential to prepare all the CAD models.

References

1. Chen W, Hao H, Hughes D, et al (2015) Static and dynamic mechanical properties of expanded polystyrene. *Materials & Design* 69:170–180. <https://doi.org/10.1016/j.matdes.2014.12.024>
2. Doroudiani S, Kortschot MT (2003) Polystyrene foams. III. Structure-tensile properties relationships. *J Appl Polym Sci* 90:1427–1434. <https://doi.org/10.1002/app.12806>
3. Gibson LJ, Ashby MF (1997) *Cellular Solids: Structure and Properties*, 2nd ed. Cambridge University Press
4. Mustafa H, Pang TY, Ellena T, Nasir SH (2019) Impact attenuation of user-centred bicycle helmet design with different foam densities. *J Phys: Conf Ser* 1150:012043. <https://doi.org/10.1088/1742-6596/1150/1/012043>

5. Michio Clark J, Post A, Blaine Hoshizaki T, Gilchrist MD (2018) Distribution of Brain Strain in the Cerebrum for Laboratory Impacts to Ice Hockey Goaltender Masks. *Journal of Biomechanical Engineering* 140:121007. <https://doi.org/10.1115/1.4040605>
6. Connor TA, Clark JM, Jayamohan J, et al (2019) Do equestrian helmets prevent concussion? A retrospective analysis of head injuries and helmet damage from real-world equestrian accidents. *Sports Med - Open* 5:19. <https://doi.org/10.1186/s40798-019-0193-0>
7. Kroeker SG, Özkul MÇ, DeMarco AL, et al (2020) Density Variation in the Expanded Polystyrene Foam of Bicycle Helmets and Its Influence on Impact Performance. *Journal of Biomechanical Engineering* 142:041012. <https://doi.org/10.1115/1.4045709>
8. Pang TY, Thai KT, McIntosh AS, et al (2011) Head and neck responses in oblique motorcycle helmet impacts: a novel laboratory test method. *International Journal of Crashworthiness* 16:297–307. <https://doi.org/10.1080/13588265.2011.559799>
9. Johannes Wilhelm, Mariusz Ptak, Eugeniusz Rusiński (2017) Simulated depiction of head and brain injuries in the context of cellularbased materials in passive safety devices. *50 Scientific Journals of the Maritime University of Szczecin* 122:98–104. <https://doi.org/10.17402/222>
10. Miralbes R, Ranz D, Ivens J, Gomez JA (2020) Characterization of cork and cork agglomerates under compressive loads by means of energy absorption diagrams. *Eur J Wood Prod.* <https://doi.org/10.1007/s00107-020-01625-7>
11. Fernandes F, Alves de Sousa R, Ptak M, Migueis G (2019) Helmet Design Based on the Optimization of Biocomposite Energy-Absorbing Liners under Multi-Impact Loading. *Applied Sciences* 9:735. <https://doi.org/10.3390/app9040735>
12. Yang Z (Joey), Zhang F, Still B, et al (2017) Physical and Mechanical Properties of Fungal Mycelium-Based Biofoam. *J Mater Civ Eng* 29:04017030. [https://doi.org/10.1061/\(ASCE\)MT.1943-5533.0001866](https://doi.org/10.1061/(ASCE)MT.1943-5533.0001866)
13. Khosroshahi SF, Duckworth H, Galvanetto U, Ghajari M (2019) The effects of topology and relative density of lattice liners on traumatic brain injury mitigation. *Journal of Biomechanics* 97:109376. <https://doi.org/10.1016/j.jbiomech.2019.109376>
14. Lee NA, Weber RE, Kennedy JH, et al (2020) Sequential Multimaterial Additive Manufacturing of Functionally Graded Biopolymer Composites. *3D Printing and Additive Manufacturing* 7:205–215. <https://doi.org/10.1089/3dp.2020.0171>
15. Ren F, Zhang C, Liao W, et al (2021) Transition boundaries and stiffness optimal design for multi-TPMS lattices. *Materials & Design* 210:110062. <https://doi.org/10.1016/j.matdes.2021.110062>
16. Ma Q, Zhang L, Ding J, et al (2021) Elastically-isotropic open-cell minimal surface shell lattices with superior stiffness via variable thickness design. *Additive Manufacturing* 47:102293. <https://doi.org/10.1016/j.addma.2021.102293>

17. Miralbes R, Higuera S, Ranz D, Gomez JA (2021) Comparative analysis of mechanical properties and energy absorption capabilities of functionally graded and non-graded thermoplastic sheet gyroid structures. *Mechanics of Advanced Materials and Structures* 1–14. <https://doi.org/10.1080/15376494.2021.1949509>
18. Najmon JC, DeHart J, Wood Z, Tovar A (2018) Cellular Helmet Liner Design through Bio-inspired Structures and Topology Optimization of Compliant Mechanism Lattices. *SAE Int J Trans Safety* 6:217–235. <https://doi.org/10.4271/2018-01-1057>
19. Shepherd T, Winwood K, Venkatraman P, et al (2020) Validation of a Finite Element Modeling Process for Auxetic Structures under Impact. *Phys Status Solidi B* 257:1900197. <https://doi.org/10.1002/pssb.201900197>
20. Khosroshahi SF, Tsampas SA, Galvanetto U (2018) Feasibility study on the use of a hierarchical lattice architecture for helmet liners. *Materials Today Communications* 14:312–323. <https://doi.org/10.1016/j.mtcomm.2018.02.002>
21. Zhang L, Feih S, Daynes S, et al (2018) Energy absorption characteristics of metallic triply periodic minimal surface sheet structures under compressive loading. *Additive Manufacturing* 23:505–515. <https://doi.org/10.1016/j.addma.2018.08.007>
22. Bhandari S, Lopez-Anido R (2018) Finite element analysis of thermoplastic polymer extrusion 3D printed material for mechanical property prediction. *Additive Manufacturing* 22:187–196. <https://doi.org/10.1016/j.addma.2018.05.009>
23. Al-Ketan O, Rowshan R, Abu Al-Rub RK (2018) Topology-mechanical property relationship of 3D printed strut, skeletal, and sheet based periodic metallic cellular materials. *Additive Manufacturing* 19:167–183. <https://doi.org/10.1016/j.addma.2017.12.006>
24. Choy SY, Sun C-N, Leong KF, Wei J (2017) Compressive properties of Ti-6Al-4V lattice structures fabricated by selective laser melting: Design, orientation and density. *Additive Manufacturing* 16:213–224. <https://doi.org/10.1016/j.addma.2017.06.012>
25. Abayazid FF, Ghajari M (2020) Material characterisation of additively manufactured elastomers at different strain rates and build orientations. *Additive Manufacturing* 33:101160. <https://doi.org/10.1016/j.addma.2020.101160>
26. Zhao M, Liu F, Fu G, et al (2018) Improved Mechanical Properties and Energy Absorption of BCC Lattice Structures with Triply Periodic Minimal Surfaces Fabricated by SLM. *Materials* 11:2411. <https://doi.org/10.3390/ma11122411>
27. Panesar A, Abdi M, Hickman D, Ashcroft I (2018) Strategies for functionally graded lattice structures derived using topology optimisation for Additive Manufacturing. *Additive Manufacturing* 19:81–94. <https://doi.org/10.1016/j.addma.2017.11.008>
28. Neff C, Hopkinson N, Crane NB (2018) Experimental and analytical investigation of mechanical behavior of laser-sintered diamond-lattice structures. *Additive Manufacturing* 22:807–816. <https://doi.org/10.1016/j.addma.2018.07.005>

29. Maskery I, Sturm L, Aremu AO, et al (2018) Insights into the mechanical properties of several triply periodic minimal surface lattice structures made by polymer additive manufacturing. *Polymer* 152:62–71.
<https://doi.org/10.1016/j.polymer.2017.11.049>
30. Yu S, Sun J, Bai J (2019) Investigation of functionally graded TPMS structures fabricated by additive manufacturing. *Materials & Design* 182:108021.
<https://doi.org/10.1016/j.matdes.2019.108021>
31. Podroužek J, Marcon M, Ninčević K, Wan-Wendner R (2019) Bio-Inspired 3D Infill Patterns for Additive Manufacturing and Structural Applications. *Materials* 12:499. <https://doi.org/10.3390/ma12030499>
32. Miralbes R, Ranz D, Pascual FJ, et al (2020) Characterization of additively manufactured triply periodic minimal surface structures under compressive loading. *Mechanics of Advanced Materials and Structures* 1–15.
<https://doi.org/10.1080/15376494.2020.1842948>
33. Higuera S, Miralbes R, Ranz D (2021) Mechanical properties and energy–absorption capabilities of thermoplastic sheet gyroid structures. *Mechanics of Advanced Materials and Structures* 1–15. <https://doi.org/10.1080/15376494.2021.1919803>
34. Mishra AK, Chavan H, Kumar A (2021) Effect of material variation on the uniaxial compression behavior of FDM manufactured polymeric TPMS lattice materials. *Materials Today: Proceedings* 46:7752–7759.
<https://doi.org/10.1016/j.matpr.2021.02.276>
35. Novak N, Al-Ketan O, Krstulović-Opara L, et al (2021) Quasi-static and dynamic compressive behaviour of sheet TPMS cellular structures. *Composite Structures* 266:113801. <https://doi.org/10.1016/j.compstruct.2021.113801>
36. Hyde S (1997) *The Language of shape: the role of curvature in condensed matter--physics, chemistry, and biology*. Elsevier, Amsterdam [Netherlands] ; New York
37. Scherer MRJ (2013) *Double-Gyroid-Structured Functional Materials: Synthesis and Applications*, 1st ed. 2013. Springer International Publishing : Imprint: Springer, Cham
38. Maran S, Masters IG, Gibbons GJ (2020) Additive Manufacture of 3D Auxetic Structures by Laser Powder Bed Fusion—Design Influence on Manufacturing Accuracy and Mechanical Properties. *Applied Sciences* 10:7738.
<https://doi.org/10.3390/app10217738>
39. Alomar Z, Concli F (2020) A Review of the Selective Laser Melting Lattice Structures and Their Numerical Models. *Adv Eng Mater* 22:2000611.
<https://doi.org/10.1002/adem.202000611>
40. Zouzias D, De Bruyne G, Miralbes R, Ivens J (2020) Characterization of the Tensile Behavior of Expanded Polystyrene Foam as a Function of Density and Strain Rate. *Adv Eng Mater* 22:2000794. <https://doi.org/10.1002/adem.202000794>

41. Miltz J, Ramon O (1990) Energy absorption characteristics of polymeric foams used as cushioning materials. *Polym Eng Sci* 30:129–133. <https://doi.org/10.1002/pen.760300210>
42. Linul E, Serban DA, Voiconi T, et al (2014) Energy - Absorption and Efficiency Diagrams of Rigid PUR Foams. *KEM* 601:246–249. <https://doi.org/10.4028/www.scientific.net/KEM.601.246>
43. Hanssen AG, Langseth M, Hopperstad OS (2000) Static and dynamic crushing of square aluminium extrusions with aluminium foam filler. *International Journal of Impact Engineering* 24:347–383. [https://doi.org/10.1016/S0734-743X\(99\)00169-4](https://doi.org/10.1016/S0734-743X(99)00169-4)
44. Benedetti M, Klarin J, Johansson F, et al (2019) Study of the Compression Behaviour of Ti6Al4V Trabecular Structures Produced by Additive Laser Manufacturing. *Materials* 12:1471. <https://doi.org/10.3390/ma12091471>
45. Maskery I, Aboulkhair NT, Aremu AO, et al (2017) Compressive failure modes and energy absorption in additively manufactured double gyroid lattices. *Additive Manufacturing* 16:24–29. <https://doi.org/10.1016/j.addma.2017.04.003>
46. Rusch KC (1969) Load–compression behavior of flexible foams. *J Appl Polym Sci* 13:2297–2311. <https://doi.org/10.1002/app.1969.070131106>
47. Guo X, Zheng X, Yang Y, et al (2019) Mechanical behavior of TPMS-based scaffolds: a comparison between minimal surfaces and their lattice structures. *SN Appl Sci* 1:1145. <https://doi.org/10.1007/s42452-019-1167-z>
48. AlMahri S, Santiago R, Lee D-W, et al (2021) Evaluation of the dynamic response of triply periodic minimal surfaces subjected to high strain-rate compression. *Additive Manufacturing* 46:102220. <https://doi.org/10.1016/j.addma.2021.102220>
49. Shi X, Liao W, Li P, et al (2020) Comparison of Compression Performance and Energy Absorption of Lattice Structures Fabricated by Selective Laser Melting. *Adv Eng Mater* 22:2000453. <https://doi.org/10.1002/adem.202000453>